Eur. Phys. J. A **30**, 215–226 (2006)
DOI 10.1140/epja/i2006-10118-5

THE EUROPEAN PHYSICAL JOURNAL A

Calorimetry

V.E. Viola[1,a] and R. Bougault[2]

[1] IUCF and Department of Chemistry, Indiana University, Bloomington, IN 47405, USA
[2] LPC/Ensicaen, 6 Bd du Maréchal Juin, 14050 Caen Cedex, France

Received: 12 June 2006 /
Published online: 25 October 2006 –

Abstract. Methods for determining the heat content E^*/A of hot nuclei formed in energetic nuclear reactions are discussed. The primary factors involved in converting raw data into thermal physics distributions include: 1) design of the detector array, 2) constraints imposed by the physics of the reaction mechanism, and 3) assumptions involved in converting the filtered data into E^*/A. The two primary sources of uncertainty in the calorimetry are the elimination of nonequilibrium emissions from the event components and accounting for the contribution of neutron emission to the excitation energy sum.

PACS. 25.40.Ve Other reactions above meson production thresholds (energies $> 400\,\mathrm{MeV}$) – 25.70.Pq Multifragment emission and correlations – 25.70.-z Low and intermediate energy heavy-ion reactions

1 Introduction

In order to describe the thermodynamic behavior of hot nuclear matter formed in energetic nuclear reactions, a knowledge of the heat content is fundamental. Stimulated by the caloric-curve measurements of the ALADiN group [1], extensive effort has been devoted to the determination of this energetic factor over the past decade. For hot nuclei the heat content is expressed in terms of the excitation energy E^*. Since nuclei are finite systems, the number of nucleons A is also necessary, so that the relevant thermodynamic quantity is E^*/A. This paper is devoted to the factors involved in evaluating E^*/A and the limitations imposed on the results due to experimental and physics constraints.

Ideally, the dynamics of the entrance channel lead to well-defined disintegrating ensembles and the calorimetric measurement of E^*/A requires an apparatus that collects the total kinetic energy (K), charge (Z) and mass (A) of all charged particles and neutrals that compose a given event. With this information each event can be reconstructed, permitting the calculation of E^* and A of the source, where

$$E^*_{source} = \sum_i K_{cp}(i) + \sum_j K_n(j) - Q(i,j) \qquad (1)$$

and

$$Z_{source} = \sum_i Z_{cp}(i), \qquad (2)$$

$$A_{source} = \sum_i A_{cp}(i) + \sum_j A_n(j). \qquad (3)$$

Here K_{cp} is the kinetic energy for all LCPs (H and He), IMFs ($3 \leq Z \lesssim 20$) and heavy residues ($A \gtrsim 20$). K_n is the neutron kinetic energy and energy of gammas, and the removal energy ($-Q$) is the negative of the reaction Q-value. All kinetic energies should be calculated in the source frame. The charge and mass of the source are given by Z_{source} and A_{source}; the charge of the emitted charged particles is Z_{cp}, and A_{cp} and A_n are the mass numbers of the charged particles and neutrons, respectively.

However, no calorimeter is perfect and, moreover, the entrance channel dynamics may lead to several sources that produce particles. Thus, in order to extract E^*/A of a given source from data, one must construct a detector filter that converts the measured distributions into final data. Among the sources of energy, charge and mass loss or contamination are:

1. acceptance limitations imposed by the construction of the apparatus and the properties of its constituent detectors [2];
2. physics uncertainties, most importantly the criteria for accepting only studied source particles that are classified as "equilibrium-like"; *i.e.*, pre-equilibrium, mid-rapidity emissions and possible contamination from other source productions (target-like and fusion events if projectile-like events are under study) must be removed from the sums for eqs. (1)-(3).
3. Measurement uncertainties, most importantly particle characterization (Z, A, angles and energy) and the characterization of the source frame used for eq. (1).

[a] e-mail: viola@indiana.edu

Table 1. Systems and detectors reviewed for calorimetry measurements.

Reaction type	Detector/Collaboration	References
$\bar{p}+A$	Berlin n/cp Ball	[3,4]
$\bar{p}, p, \pi, {}^3\mathrm{He}+A$	ISiS	[5,6]
$p, {}^4\mathrm{He}, C+A$	FASA	[7]
$A+C$	EOS	[8,9]
$A+A$	ALADiN	[1,10]
$A+A$	INDRA	[11]
$A+A$	TAMU	[12,13]
$A+A$	Chimera	[14]
$A+A$	Laval array	[15]
$A+A$	Superball	[16]
$A+A$	Multics	[17–19]

4. Finally, since no two-detector arrays have the same acceptance, differences in procedures for converting the filtered data into E^*/A must be examined.

In the following sections, these issues are surveyed along with their inherent uncertainties. The analysis is drawn from those references in table 1, which are representative (but not complete) examples of the procedures currently employed in nuclear calorimetry.

2 The detection filter

The existing multifragmentation detector arrays are of various types. Most charged-particle detection involves some combination of silicon, gas ionization chamber and CsI scintillator telescopes for Z (and in some cases A) identification [3–7,11,12,14,15]. The EOS experiment [8, 9] employed a time projection chamber (TPC) and ALADiN utilized a magnetic spectrometer [1,10], both coupled to several detector arrays. Neutrons have been measured with large tanks of Gd-loaded scintillator liquid and via time-of-flight techniques [3,4,16]. Few experiments have been performed with simultaneous Z and A identification for the entire multifragmentation yield. For relativistic beams, the EOS TPC is well suited for complete Z and A identification in the forward laboratory hemisphere and the ALADiN experiments permit A detection over a significant mass range. Medium- and heavy-fragment identification by most other arrays relies on mass balance techniques and/or partial information (A or Z), with N/Z assumptions. In developing a reliable detector filter, several factors must be considered, as enumerated below. The filter must then be tested to ensure that it reproduces input from an appropriate simulation.

2.1 Solid-angle acceptance

In constructing any detector array, allowance must be made for beam entry/exit ports and any shadowing by the target. For light-ion reactions, for which the laboratory angular distributions are nearly isotropic, target shadowing must be treated carefully. For inverse kinematics or $A+A$ reactions, the effect of the exit port dead solid angle is projectile energy dependent. This effect may be controlled for high-energy beams by using a magnet. In any case the resulting geometric-acceptance factor must then be applied to all events, which due to fluctuations, may either over- or under-correct the data. For most detectors, geometric acceptance ranges from about 75% to the nearly complete acceptance for the EOS TPC in inverse kinematics. But those numbers should be reconsidered when speaking of real acceptance since the solid-angle acceptance depends on impact parameter and type of particle.

2.2 Detector granularity

Since the final states in multifragmentation reactions may involve large numbers of particles, high detector granularity ($N > 100$) is essential to minimize multiple-hit misidentification of fragments. In addition, angular information is required to test whether events classified as "equilibrium-like" meet the isotropic emission standard for a randomized system and is fundamental to rebuild the studied source velocity. The detector granularity and the angular resolution of a detector are technically different because they are related to different issues.

2.3 Detector characteristics —charged particles

The technical challenge of charged-particle detection is related to the large energetic range of particle detection and the necessity of identifying everything from light charged particles up to heavy residues.

– *Energy identification thresholds:*
Ideally, for eqs. (1) and (2) Z and A identification of the products is required. Practically, this is almost done for light charged particles and light IMFs with an energetic threshold that depends, for example on the ΔE-E technique, on the thickness of the ΔE. Below the threshold and for all other charged particles either A (ΔE-E technique) or Z (time-of-flight technique) remains unknown and mean values are used in the calorimetry.
– *Energy thresholds:*
The low-energy component of spectra measured with ΔE-E particle identification telescopes is constrained by the thickness of the ΔE element. Lowest thresholds are obtained with gas ionization chambers, essential for light-ion–induced reactions or excited target-like source reconstruction. The kinematic boost for fragments produced in heavy-ion reactions permits the use of higher stopping power, Si and CsI ΔE elements in the forward direction. Since the energy threshold depends on the detected species, this may affect the overall real detector acceptance. Ideally, corrections to the energy sum must be made for the missing part of the spectrum due to threshold effects.

– *Detector resolution:*
Si semiconductor detectors provide the highest energy resolution for the determination of energy loss and total energy K. For this reason Si-Si telescopes can provide both Z and A information for a significant range of the multifragmentation spectrum, limited by the minimum ΔE thickness and maximum E thickness. Si detectors are also used for time-of-flight A identification. Because of their minimum stopping power, gas ionization chambers are most effective as ΔE detectors for fragments with low kinetic energy per nucleon but usually do not yield both Z and A identification. Although CsI provides the poorest energy resolution, the ability to form very thick crystals makes it ideal for detecting the most energetic particles. Depending on the energy of the emitted particles, TPC measurements usually yield energy resolution intermediate between Si and CsI for IMFs and heavier fragments. In addition, plastic scintillators and pulse-shape discrimination have been employed, as well as silicon pulse-shape analysis, to identify fragments.

2.4 Detector characteristics —neutrons

The greatest experimental uncertainty in determining the total kinetic-energy sum is the contribution from neutron emission, for which multiplicities are greater than or comparable to charged particles. The energy associated with gamma rays is usually assumed to be small. The neutron kinetic-energy spectrum is measured via time-of-flight techniques, using fast plastic/liquid scintillators. Such measurements sample only a small fraction of 4π because of the spatial limitations imposed by the flight path. Hence, they yield only limited multiplicity information. Neutron multiplicities and charged-particle correlations have been determined with $\approx 4\pi$ tanks of Gd-loaded liquid scintillator [4,12,16]. Neutron detection must be corrected for energy-dependent efficiency losses, which contribute to the multiplicity uncertainty. When neutrons are not detected, mean values for neutron multiplicity and total neutron kinetic energy are assumed. In the case of full identification of the source charged products, the neutron multiplicity is accessible via a source N/Z hypothesis on an event-by-event basis. For the mean total neutron kinetic energy, several techniques based on proton characteristics or on experimental results or on average effective-temperature estimates are employed.

2.5 Replacement of unmeasured quantities

As has been described, there exist several methods to replace an unmeasured quantity in eqs. (1) and (2). Each method has its own advantage or disadvantage depending on the experimental context and the best choice depends on the goal of the measurement. Therefore, caution should be taken by keeping only conservative hypotheses, controlled with simulations taking into account the detector acceptance.

2.6 Statistics

The total number of events in the case of highly excited nuclei ($E^*/A \geq 2\,\mathrm{MeV}$) is a function of both the maximum event rate of the detector array and the availability of accelerator time. TPC and neutron tank measurements are limited in counting rate, so statistics are usually low. Detector array studies of $A+A$ reactions exhibit a wide range of statistics, depending on the number of systems studied in a finite amount of accelerator time. Most of the light-ion data have accumulated large numbers of events by using secondary beams over long (months) running time. Since the multifragmentation yield decreases with increasing excitation energy, the accumulation of high statistics is an important factor in determining reliable distributions.

3 Physics issues

In addition to mechanical and detector response contributions to the filter, several physics issues must be addressed, the most important of which is the selection of "equilibrium-like" events. The time evolution of nuclear reactions above the Fermi energy extends from the initial collision phase to an eventually randomized state that decays statistically. Particle emission occurs at all stages as translational projectile energy is converted into internal excitation energy. Selection of only those emissions that have a statistical origin is therefore a nontrivial problem. Other physics issues also come into play; *e.g.* neutron-proton multiplicity correlations, kinematics effects on the event reconstruction process in $A+A$ and inverse kinematics reactions, and the primary N/Z ratio of the emitted fragments. Below, these contributions to the filter are discussed.

3.1 Pre-equilibrium and mid-rapidity emission

Two essential first-order tests of a randomized system are the Maxwellian nature of its spectra and the forward-backward symmetry of its particles in the system frame. This is completely true when the collision dynamics lead to a unique fully equilibrated source of particles. It is not necessarily true for a deformed source or when Coulomb repulsion effects occur within the presence of another source of particles or in the presence of collective effects. Last but not least, the characterization of the source frame velocity is of prime importance for the angular symmetry test, where in some conditions this test may be used for determining the source velocity.

In figs. 1-5 spectra are shown for light-ion–induced reactions at GeV energies. These spectra best illustrate the prompt *vs.* statistical emission ambiguity, since there is only a single emitting source and the difference between the laboratory and center-of-mass velocities is small ($\approx 0.01\ c$). Figure 1 shows neutron spectra at a far backward angle for reactions of 1.2 GeV antiprotons on several targets [3,4]. Two components are present: a low-energy Maxwellian peak and an exponential high-energy tail. The

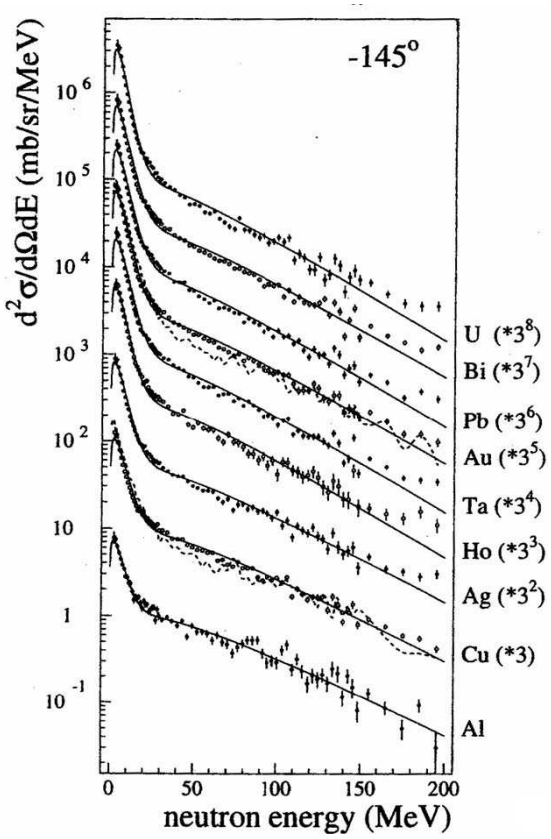

Fig. 1. Neutron kinetic-energy spectra at 145 deg for several target nuclei bombarded with 1.2 GeV antiprotons. Taken from ref. [20].

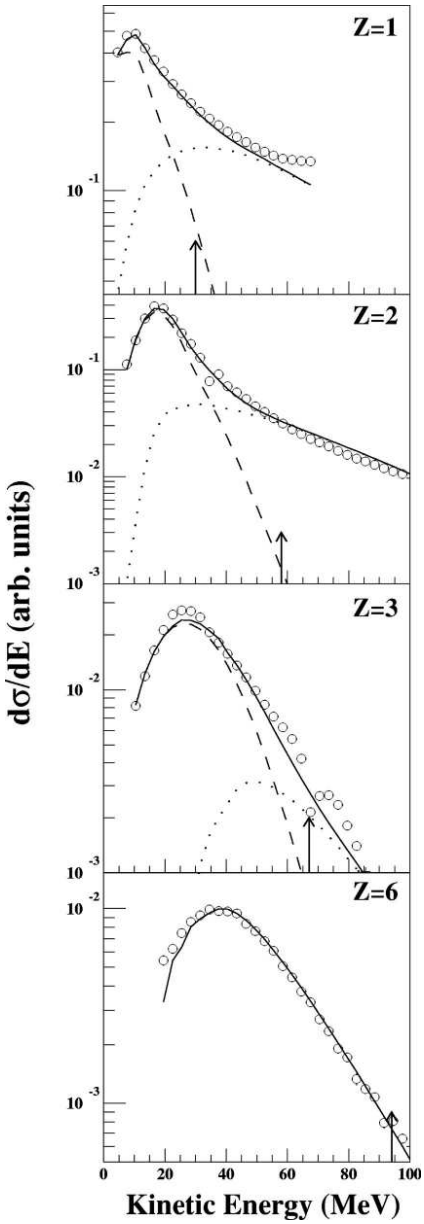

Fig. 2. Angle-integrated kinetic-energy spectra for $Z = 1$, 2, 3 and 6 particles observed in the 8.0 GeV/c $\pi^- + {}^{197}$Au reaction. Lines are the result of a two-component moving-source fit composed of a thermal source (dashed line), nonequilibrium source (dotted line) and their sum (solid line). Taken from ref. [6].

former is associated with "equilibrium-like" behavior and the latter with pre-equilibrium emission. Separating these two components on an event-by-event basis is not a transparent procedure. Figure 2 shows inclusive spectra for LCPs and IMFs measured in the 8 GeV/c $\pi^- + {}^{197}$Au reaction [6]. These spectra have been decomposed using a two-component moving-source model that assumes a statistical model for the low-energy component (dashed line) and an arbitrary Maxwellian function for the high-energy tail (dotted line). Pre-equilibrium emission is seen to be primarily important for LCPs and decreases in significance as the fragment charge increases.

In fig. 3 the angular dependence of the spectra is shown, along with the moving-source decomposition. Pre-equilibrium emission is forward-focused, whereas the statistical component (when integrated) is nearly isotropic in the lab system. By demanding forward-backward isotropy of the statistical component, the average source velocity can be determined, as well as the fragment energy at which the pre-equilibrium contribution is a negligible contribution to the total yield (cutoff energy). The average source velocity and cutoff energy can be determined from moving-source fits to the data. These are then incorporated into the filter, using a Z-dependent function for the cutoff energy.

As examples of how the separation between statistical and pre-equilibrium affects the determination of E^*/A, fig. 4 compares the excitation energy distribution for the $\pi^- + {}^{197}$Au reaction using both the EOS cutoff energy of $K_{cp}/A = 30$ MeV for all particles [8,9] and that employed by ISiS, $K = 30$ MeV for protons and $K_{cp} = 9Z + 30$ MeV for higher fragment charges [21]. The EOS prescription enhances the probability for high E^*/A values, leading to the difference of nearly 200 MeV at the 1% probability level. (In all other regards the 1 GeV ^{197}Au + ^{12}C results from EOS are consistent with the 8 GeV/c $\pi^- + {}^{197}$Au results from ISiS.)

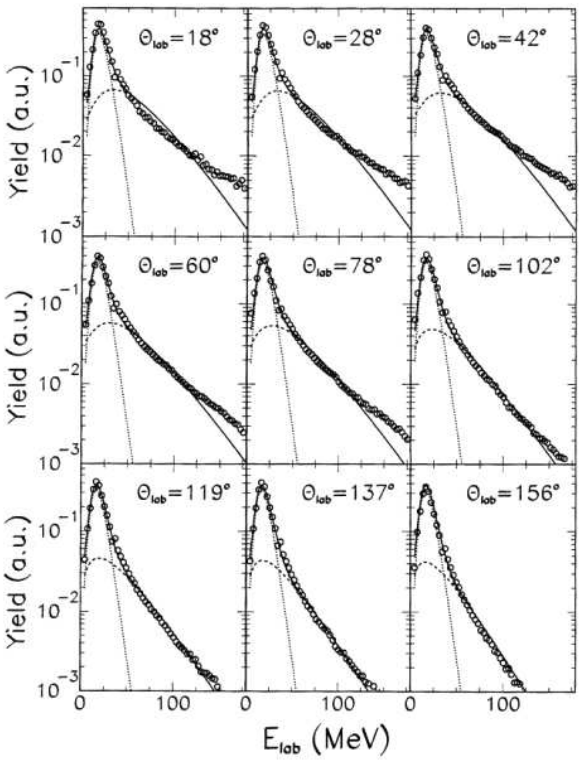

Fig. 3. Alpha-particle kinetic-energy spectra as a function of the angle, from ref. [6].

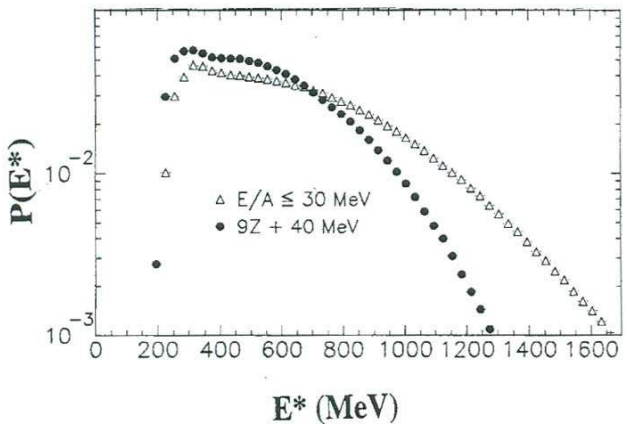

Fig. 4. Comparison of excitation energy distributions for the same experimental data set analyzed with the thermal cutoff energies of refs. [6] (circles) and [9] (triangles).

The pre-equilibrium/statistical separation process is further complicated by the evolution of the spectra with E^*/A as shown in fig. 5. Here H and He spectra, which dominate the pre-equilibrium yield, are shown for $E^*/A =$ 2–4, 4–6 and 6–9 MeV bins. The ISiS cutoff assumptions were derived from the lower-energy bin. However, as E^*/A increases, the spectra evolve into a single Maxwellian distribution, so that separation of the two components becomes more ambiguous.

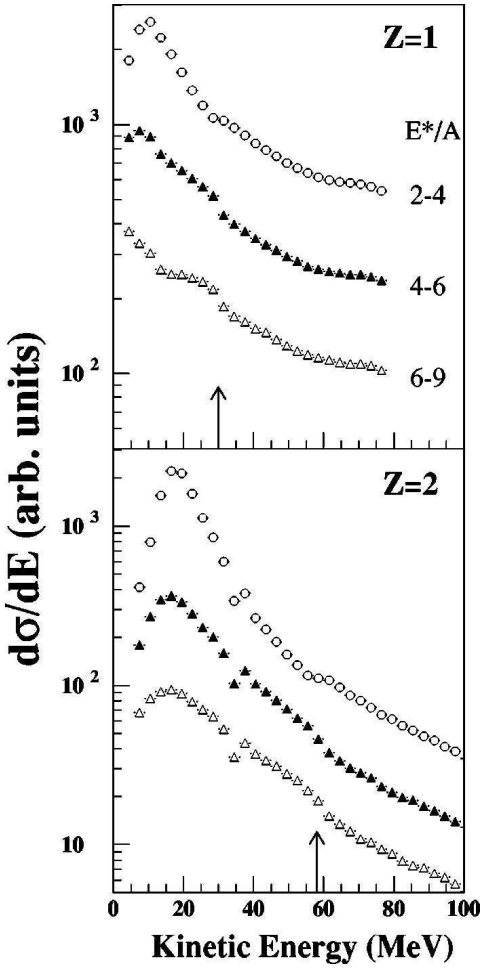

Fig. 5. Kinetic-energy spectra for $Z = 1$ and 2 nuclei as a function of excitation energy for the 8.0 GeV/u reaction. From ref. [6].

For $A + A$ reactions the situation is complicated by the existence of three sources: the projectile-like, target-like and mid-rapidity ones, each of which is then subjected to the same constraints as for light ions. The behavior of the three sources is illustrated in fig. 6, which shows invariant cross-section distributions for $Z = 3$, 6 and 9 fragments as a function of bombarding energy for peripheral ^{197}Au + ^{197}Au data from the INDRA@GSI Collaboration [22]. The separation of the Coulomb rings for the projectile-like source (high y) from the target-like source (low y) becomes increasingly distinct as the bombarding energy increases. For $Z = 3$ the pre-equilibrium skewing of the spectra along the beam axis ($x = 0$) is apparent. For $Z = 6$ and 9 this contribution becomes less important. At lower bombarding energies, the mid-rapidity source masks the projectile-like and target-like statistical spectra, complicating their separation, a procedure that entails the same type of arbitrary assumptions that exist for the light-ion data.

The effect of assumptions about nonequilibrium emission is presented in fig. 7 for peripheral ^{197}Au + ^{197}Au re-

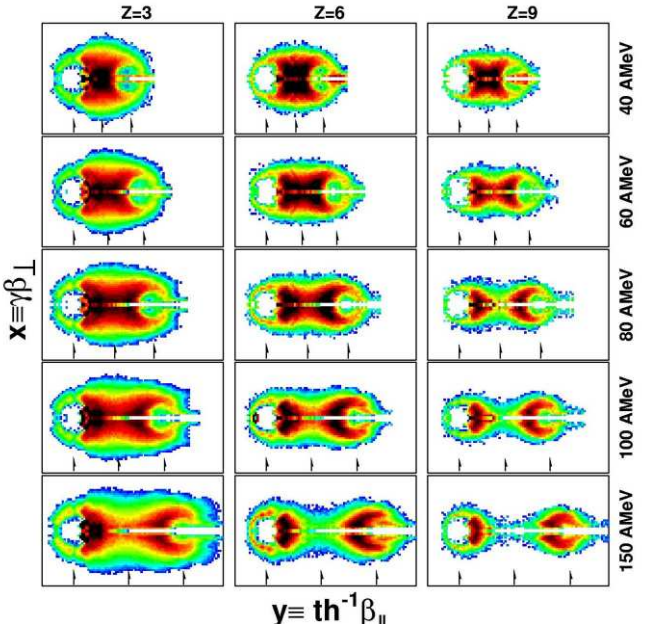

Fig. 6. Invariant cross-section plots for $Z = 3$, 6 and 9 fragments as a function of bombarding energy for the ^{197}Au + ^{197}Au reaction [22].

action energies of 600, 800 and 1000 GeV, data obtained by the ALADiN group [23]. In the caloric curve shown in the top panel, the E^*/A distribution extends up to 25 MeV for the 1000 A MeV data, and the two caloric curves are not consistent. In the central panel, the relative contributions of neutrons, LCPs and IMFs indicate that the nonequilibrium contributions to the spectra grow significantly between 600 A and 1000 A MeV. As shown in the bottom panel, when corrections are made to eliminate nonequilibrium components, the caloric curves overlap, with maximum E^*/A values reduced to $E^*/A \approx 12$ MeV for both bombarding energies.

For $A + A$ central collisions at lower energies (see for example [24]), a single statistical source can be identified and concerning light charged particles, cuts are applied in order to take into account particle emission at different stages. In general the more massive particles are assumed to originate from a single source, even though their angular distributions in the source frame present some anisotropy. This so-called source deformation depends on bombarding energy. Sophisticated event selections based on isotropy criteria and only operatives in case of quasi-complete detection are also used in order to extract from the central events almost fully equilibrated events. Even in this case, cuts are applied to light charged particles for excitation energy measurement because of pre-equilibrium emission.

3.2 Neutrons

The evaluation of E^*/A via eqs. (1) and (2) requires a knowledge of the kinetic energy and multiplicity of

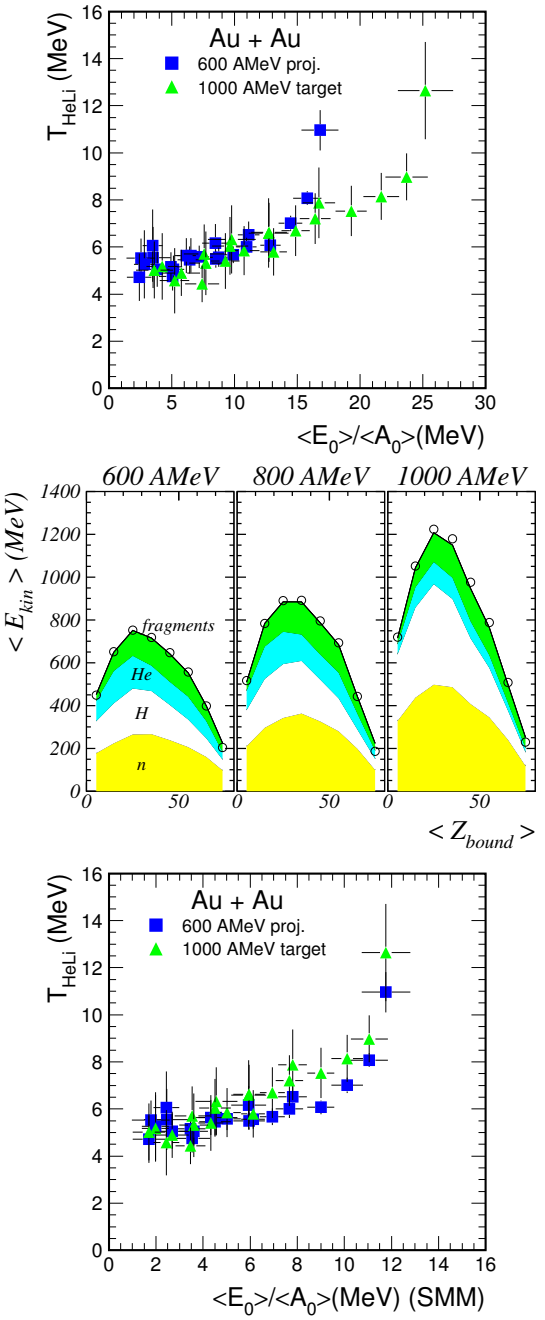

Fig. 7. Top panel: caloric-curve comparison for $E/A = 600$ and 1000 MeV ^{197}Au + ^{197}Au reaction, uncorrected for non-thermal effects. Center panel: average fragment kinetic energies for $E/A = 600$, 800 and 1000 MeV as a function of Z_{bound}. Bottom panel: caloric-curve comparison when corrected for non-thermal effects [23].

the neutrons in an event. Because of the inherent difficulties in measuring neutrons, as discussed previously, only few measurements exist that measure neutrons and charged particles simultaneously. Important examples are the studies carried out with the Berlin Ball [3,4], the Rochester Superball [16], the ORION detector [25] and the Texas A&M NIMROD [12] systems. For those ar-

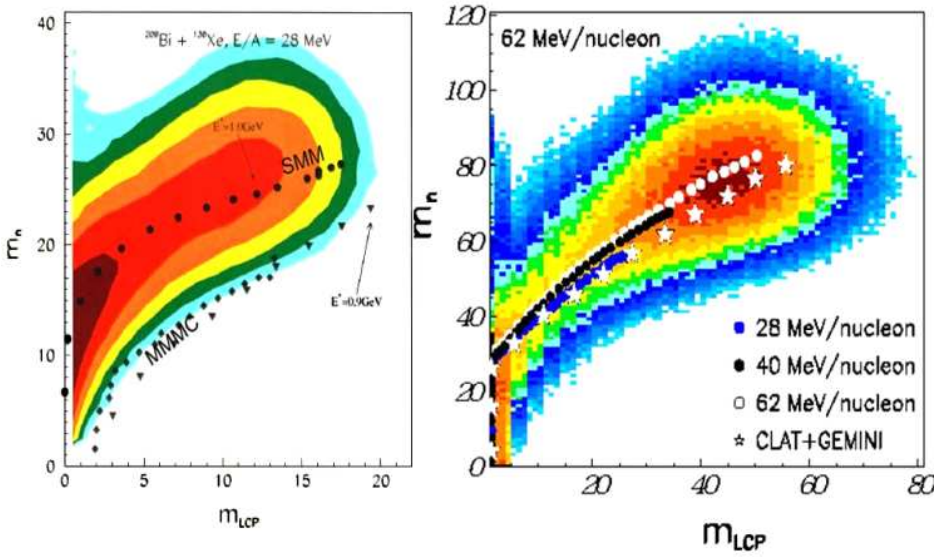

Fig. 8. Experimental correlations between neutron and light-charged-particle multiplicities from the ^{209}Bi + ^{136}Xe reactions [26]. The left panel shows a correlation compared with SMM and MMMC predictions; the right panel compares results for different bombarding energies.

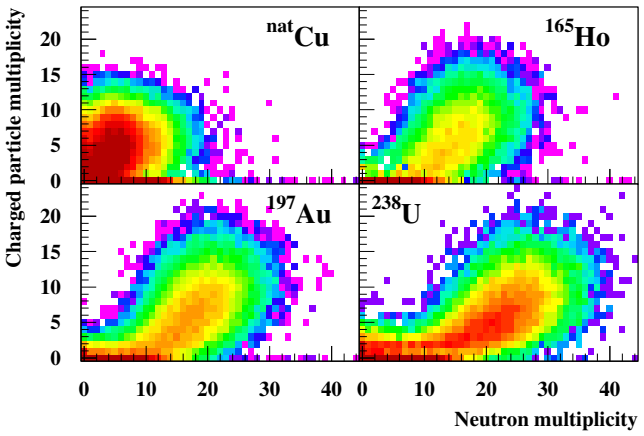

Fig. 9. Experimental neutron *vs.* charged-particle multiplicity for 1.2 GeV antiprotons on several targets. Taken from ref. [4].

rays that detect only charged particles, the existing measurements of neutron-proton multiplicity correlations and spectra must be relied upon to estimate the missing neutron contribution to E^*/A. Neutron spectra were shown in fig. 1 which emphasizes the fact that neutrons may also originate from pre-equilibrium emission.

In figs. 8 and 9 the neutron-light-charged particle multiplicity correlations are compared for $A + A$ and light-ion reactions. Two systems are shown: 28 MeV/A Xe + Bi [26] and 1.2 GeV $\bar{p}$ + several targets [3,4], respectively. Both cases behave similarly, with a target mass-dependence (fig. 9) that favors an increasing growth in the n/LCP ratio with increasing target mass. The total particle multiplicity is known to be strongly correlated with excitation energy. For heavy targets the neutron multiplicity increases rapidly with excitation energy up to $E^*/A \approx 2$ MeV, while charged-particle emission remains low due to Coulomb inhibition. At higher excitation energies, the probability for additional neutron emission is approximately balanced by LCP emission. The left part of fig. 8 compares the Xe + Bi multiplicity correlation with the average predicted by two multifragmentation models, SMM [27] and MMMC [28]. It was assumed that neutrons and light charged particles are emitted from excited projectile- and target-like sources containing total excitation energy of 0.9 GeV or 1.0 GeV. Without entering into details of models and data comparisons, we see that the mean trend of the correlation can be understood within the framework of an equilibration scenario. The effect of increased bombarding energy on the n/LCP correlation is indicated for the Xe + Bi case in the right part of fig. 8. No strong dependence is observed and here again a statistical de-excitation model (GEMINI [29]) is able to reproduce the mean trend.

For heavy targets the relative insensitivity of the n/LCP ratio to colliding system or bombarding energy, as well as the general agreement with models, provides guidance in accounting for the missing neutron fraction of E^*/A in arrays that measure only charged particles. Various approaches have been followed: use of model calculations calibrated to the LCP multiplicity, or direct use of the experimental multiplicity correlation centroids. An alternative is to employ a mass balance approach, as determined from the experimental event structure. In this latter event-by-event method the neutron multiplicity is determined by mass conservation assuming the N/Z ratio of the studied source. This requires a reliable determination of total Z.

Figure 10 illustrates the effectiveness of such techniques, using the 1.2 GeV $\bar{p}$ + ^{197}Au results [3,4]. SMM (dotted curve) and SIMON-evaporation [30] (dashed line), both statistical models, provide a reasonable description

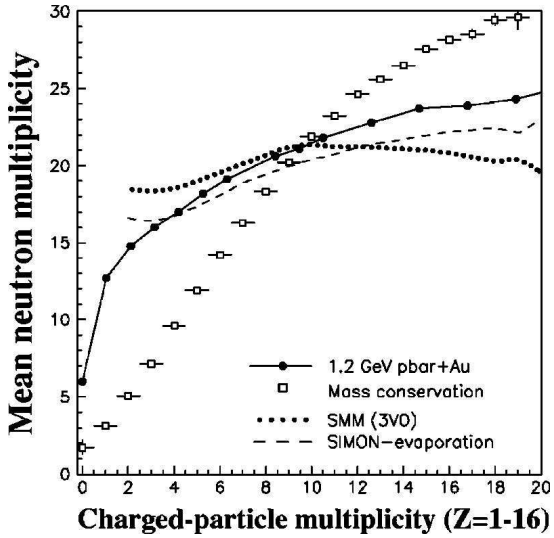

Fig. 10. Comparison of neutron *vs.* charged-particle multiplicity for the 1.2 GeV antiproton + ^{197}Au reaction with SMM, SIMON-evaporation and mass balance assumptions as indicated in the legend. Taken from ref. [6].

of the data for $M_{\rm LCP} \geq 3$ ($E^*/A \approx 2$ MeV), considering that statistical models do not describe the pre-equilibrium particle emission. Mass conservation (open squares) is not satisfactory in this case, although in some instances the nature of the data may provide a more satisfactory fit.

Finally, even in case of neutron detection, the primary difficulty in the determination of the neutron contribution to E^* and the source mass A_{source} is that the neutron tanks provide multiplicity information (good for A_{source}) but not neutron energies, while the time-of-flight method provides energies (good for K_n) but only limited multiplicity data. By use of LCP-calibrated models, it is possible to obtain a reasonable approximation to the total excitation energy contributed by neutrons. However, in doing so, one is employing averages that fail to introduce fluctuations in M_n and K_n.

3.3 Additional factors

While non-equilibrium emission and neutron emission constitute the major sources of uncertainty in the determination of E^*/A, several other factors must be taken into account, as discussed in the following.

– *Source reconstruction:*
Among the various multifragmentation programs, calculations of the properties of the emitting source —charge, mass and velocity— are usually detector-array–dependent. For light ion + A reactions, for which there is only one source, the reconstruction depends on the acceptance of the array. The EOS TPC measurements provide nearly complete charged-particle detection [9], as shown in the left part of fig. 11, from which the statistical component of an event can be extracted.

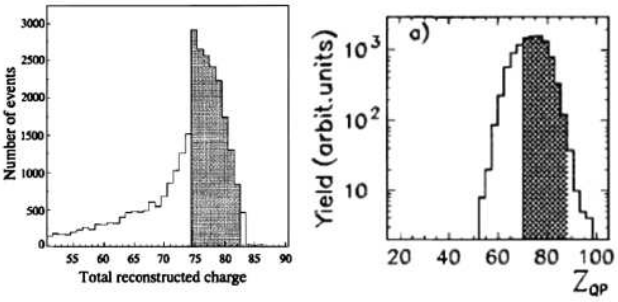

Fig. 11. Quasiprojectile reconstructed charge distributions for EOS (left part, taken from ref. [9]), and for MULTICS-MINIBALL (right part, taken from ref. [17]). In both cases the initial projectile charge is $Z_P = 79$. The shaded areas give the events used for the calorimetric and thermodynamic analyses.

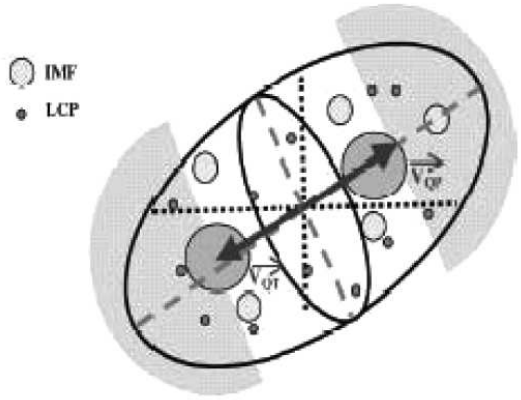

Fig. 12. Schematic representation of the momentum tensor analysis to reconstruct the reaction plane (see text).

For $A + A$ reactions some authors utilize a center-of-mass tensor analysis in order to reconstruct the reaction plane, schematically shown in fig. 12. This procedure, only adopted in the case of a nearly perfect detection, is used to isolate the fragments of the studied source. For the schematic example of fig. 12, the forward center-of-mass emitted fragments are assumed to originate from the excited projectile-like source, and only light charged particles emitted in the forward hemisphere of the source are taken into account for calorimetry because of pre-equilibrium effects at mid-rapidity. Going back to fig. 6, we can see that mid-rapidity emission concerns also light fragments and thus, depending on the reaction and the experimental apparatus, additional criteria and/or checks are used for accepting only studied source fragments that are classified as "equilibrium-like". As an example, total-charge results for projectile-like fragments from ^{197}Au + ^{197}Au studies of the MULTICS/MINIBALL are presented in the right part of fig. 11 [17]. In nearly all cases, the emitting-source mass is determined from the A/Z ratio of the heavy collision partner(s). The velocity of the statistical source is determined as the vectorial sum of fragment velocities.

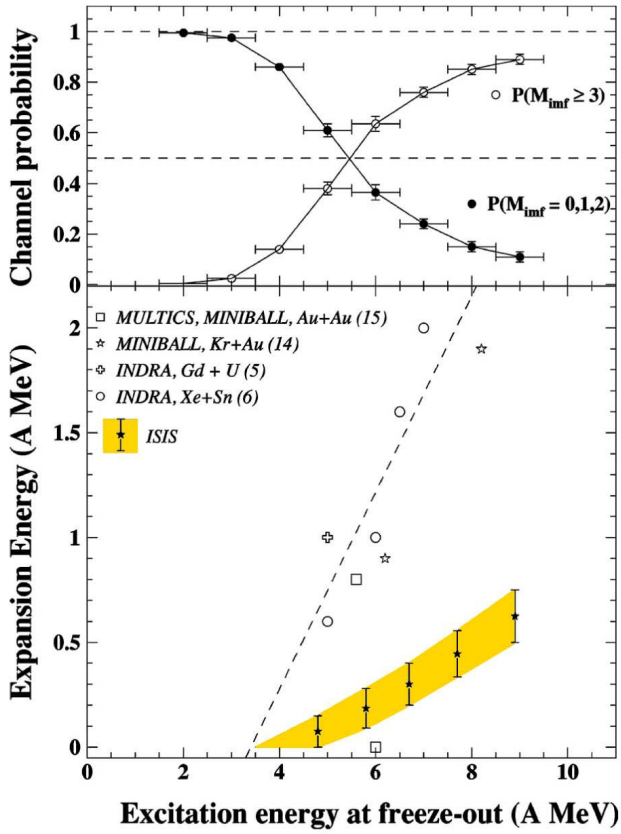

Fig. 13. Upper panel: decay channel probability for multiplicities $M \leq 2$ and $M \leq 3$. Lower panel: extra radial expansion energy for light-ion–induced reaction (yellow band) and several heavy-ion reactions, as indicated in the legend. Taken from ref. [31].

Representative protocols for evaluating the source properties are described in the next section.

– *Primary-fragment N/Z ratio:*
In the framework of statistical multifragmentation, to trace back the freeze-out stage of an event, it is necessary to know the mass and the charge of primary fragments before secondary decay. This information is not necessary for calorimetry but it is relevant to measure, for example, the mass and volume of the source. In most cases, only the fragment charge is measured for all but the lightest elements. Various approaches have addressed the conversion of the data to primary yields. One is to use the N/Z ratio of the cold fragments, the composite system, or some combination of the two. Another is to use the N/Z ratio of IMFs emitted in reactions of protons with heavy nuclei at energies below 500 MeV, where secondary emission should be small.

– *Collective energy:*
Finally, any internal energy used to expand/deform or rotate the hot source, must be subtracted from the excitation energy sum of eq. (1) in order to access thermodynamic properties of nuclear systems. As shown in fig. 13, for light-ion reactions this is a small, but non-negligible contribution at high excitation energies [31]. For $A + A$ reactions, compression effects produce considerable expansion and therefore can contribute a significant amount to the E^* sum at high excitation energies. This correction also accounts in part for the bombarding energy dependence of E^* shown in fig. 7. The amount of collective energy is generally deduced from data-model comparisons. In the case of expansion, the comparison is based on kinetic properties of the fragments and thus is dependent on model assumptions about the source volume since Coulomb repulsion is acting [19]. A and Z fragment identification over a wide range, as well as correlation measurements, could disentangle this problem.

4 E*/A protocols

The procedures for converting measured data to E^*/A differ for every multifragmentation experiment. Once detector calibration and filter development are complete, the salient variables can be applied to eqs. (1) and (2). In this section, several methods are described that are representative of the approaches that have been employed.

4.1 Model-based calorimetry

In the $\bar{p}$ studies of the Berlin Neutron/Silicon Ball [3, 4], E^* is determined by comparison of the light-charged particle multiplicity with that predicted by the evaporation code GEMINI [28] at a given excitation energy. Since IMF multiplicities are rarely greater than unity in this experiment, the use of an evaporation code is appropriate. For the higher-energy LCP + A studies employed by the FASA group, an empirical parameter α is obtained from the comparison of observed charged-particle multiplicities with the multiplicity distribution predicted by a hybrid RC + SMM model [32]. The excitation energy is then taken to be a function α times the predicted excitation energy. For experiments with good fragment detection, the element distribution (or the distribution of the biggest fragment) is used to deduce the mean excitation energy and size of the source. Genuine distributions of source characteristics (size, excitation energy, volume, ...) of collected event ensembles are accessible via backtracing procedures. In both cases this is done with data-model comparisons and event-by-event information is not accessible.

Below, we summarize the calorimetry procedures used in several representative systems that calculate E^*/A on an event-by-event basis.

4.2 Calorimetric protocols

In this section we schematically review different assumptions that have been employed in the literature to perform the calorimetric measurement. They include both corrections for the incomplete detection (neutron multiplicity

and energy, masses of heavy products) and techniques to separate pre-equilibrium and source mixing contaminations, as we have discussed in the previous sections. For more details about the procedures and their justification, we refer the reader to the original publications of the different collaborations. As a general statement, the validity of a calorimetric protocol is usually tested from an extensive use of statistical as well as dynamical simulations using realistic models [11,19]. For example in the case of the MULTICS detector, the input energy of SMM simulations, filtered using the same calorimetric protocol as data, is reproduced within 10% in the multifragmentation regime [19]. A similar performance can be associated to the INDRA detector [11].

– *EOS*:
In the analyses of the data obtained with the EOS detection system [8,9], the total charge of the studied source is estimated from the initial projectile charge by subtracting pre-equilibrium particles and fragments identified according to a cutoff energy prescription (see sect. 3.1). A number M_{cp}^{neq} of nonequilibrium charged products of charge Z_i^{neq} is thus defined event by event, leading to

$$Z_{source} = Z_{proj} - \sum_i Z_i^{neq}, \tag{4}$$

$$A_{source} = A_{proj} - \left(\sum_i Z_i^{neq} + 1.7 M_{cp}^{neq} \right). \tag{5}$$

Once the source size is known, the neutron multiplicity, M_n, can be inferred from mass conservation, while the average neutron energy, K_n, is estimated via an effective temperature T obtained within a Fermi-gas ansatz with a level density parameter $a = A/13\,\mathrm{MeV}^{-1}$:

$$M_n = A_{source} - \sum_i A_i^{thermal}, \tag{6}$$

$$\langle K_n \rangle = M_n \cdot \frac{3}{2} T. \tag{7}$$

– *ISiS*:
In the case of the ISiS detector [5,6] the procedure is similar to that of EOS, as discussed above, except that excited target-like residues are studied:

$$Z_{source} = Z_{target} - \sum_i Z_i^{neq}, \tag{8}$$

$$A_{source} = A_{target} - \left(\sum_i Z_i^{neq} + 1.93 M_{cp}^{neq} \right). \tag{9}$$

Since heavy residues are not detected, it is assumed that all missing charge resides in a single fragment, an assumption that is in good agreement with the EOS data and SMM simulations. Neutron multiplicities have been calibrated by the measured neutron-charged particle correlations of ref. [4] and kinetic energies were based on both Fermi gas and model simulation results. The IMF mass A_{IMF} is estimated based on the data of ref. [33], with the assumption that no charged-particle decay of IMFs has occurred. An overall geometrical efficiency correction is also applied.

– *INDRA and MULTICS quasiprojectile*:
Such a correction is not applied to INDRA data since the complete Z identification over 4π allows the selection of events with complete charge. Completeness conditions can vary from 70% to 90% in the different analyses and are often complemented by completeness condition of linear momentum. For MULTICS data the completeness condition is 90% and good Z identification of all emitted products is effective in the forward direction (up to about 30 degrees in the laboratory frame). We have already seen in fig. 6 that at low incident energies in the Fermi-energy range the kinematic distinction between different emission sources is blurred. The contamination from non-quasiprojectile sources is minimized by selecting as the QP i) only forward-emitted fragments (IMFs and heavy residues) via a tensor analysis, and ii) only light charged particles forward emitted in the source frame:

$$Z_{source} = \sum_i Z_i^{\mathrm{IMF+HR}} + 2 \sum_i Z_i^{\mathrm{LCP}}, \tag{10}$$

$$A_{source} = (A/Z)_{proj} \cdot Z_{source}, \tag{11}$$

$$M_n = A_{source} - \sum_i A_i^{\mathrm{IMF+HR}} - 2 \sum_i A_i^{\mathrm{LCP}}. \tag{12}$$

In these expressions, all sums over IMFs and HR are restricted to the forward hemisphere in the center-of-mass frame, while the sums over LCPs are restricted to the forward hemisphere in the reconstructed QP frame. Concerning the neutron kinetic energies, three different prescriptions have been shown to give comparable results [11]:

$$\langle K_n \rangle = bT, \tag{13}$$

$$\langle K_n \rangle = \langle K_{Z=1} \rangle - 3.5\,\mathrm{MeV}, \tag{14}$$

$$\langle K_n \rangle = M_n \cdot \frac{3}{2} T. \tag{15}$$

For the first K_n prescription the b parameter varies from $b = 1$ to $b = 2$ depending on excitation energy.

– *INDRA central*:
For INDRA symmetric central collisions the same QP-prescription has been used, but i) all detected IMFs and heavy residues have been attributed to the source, ii) the retained LCPs are those emitted between 60 degrees and 120 degrees in the center-of-mass frame and the A/Z ratio is that of the total entrance channel.

– *TAMU central*:
For asymmetric systems central collisions detected by TAMU experiments cited above [12,13], the studied source corresponds to target-like sources. The selected events correspond to central events (multiplicity cut). Three sources are present: the projectile-like, target-like and a hypothetical source whose velocity corresponds to the velocity of the nucleon-nucleon collision frame. The data rely on identification of p, d, t, ^{3}He,

^{4}He and of $3 < Z < 14$ elements. The neutron multiplicity is measured. A three-source fitting procedure is applied to energy spectra (with efficiency corrections) to obtain the size of the target-like source and the equilibrated target-like neutron multiplicity (M_n) out of the total neutron multiplicity:

$$\langle K_n \rangle = M_n \cdot \frac{3}{2} T; \qquad T = 4 - 4.7\,\mathrm{MeV}. \tag{16}$$

– *ALADiN*:
For ALADiN experiments cited above, the collision of the relativistic projectile and the target leads to a projectile spectator, a target spectator and a fireball whose size is increasing with centrality. The studied source is the forward-emitted projectile spectator whose size is decreasing with centrality. The selection among detected source particles is based on a rapidity (y) cut and a bombarding energy-dependent angular cut. Neutrons are detected by the apparatus but $Z = 1$ particles are not. The He isotopes are not identified over the full solid angle. Therefore ALADiN does not use eqs. (1) and (2) on an event-by-event basis but rather uses them with mean assumptions for unknown quantities to extract a mean value. The data are divided into Z_{bound} (sum of selected Z from He up to projectile size) ensembles and for each ensemble a mean calorimetry is applied.
– *Alternative method*:
An alternative method relative to eq. (1) to estimate the excitation energy is to measure the source velocity. Its validity is based on the reaction mechanism which is at the origin of the source excitation. Complete or incomplete fusion of asymmetric systems (mass tranfer) or a pure binary collision mechanism provide a link between E^* and the source velocity [14]. Because precise measurements of particle angles, masses and energies are needed, this method is used as a check after using eqs. (1)-(3) [17].

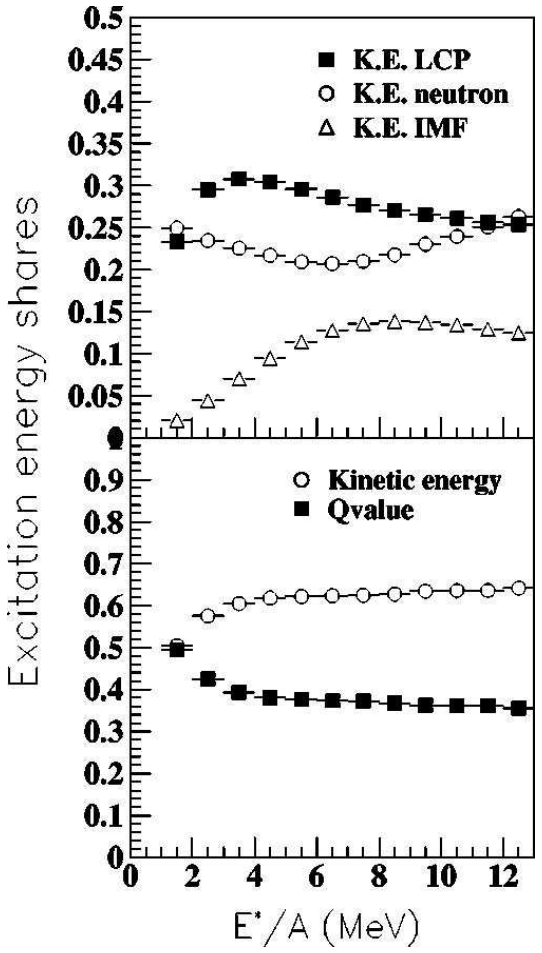

Fig. 14. Upper panel: relative kinetic-energy contributions to the excitation energy for neutrons, LCPs and IMFs as a function of excitation energy. Lower panel: relative contributions to the excitation energy from total kinetic energy and removal energy, as indicated in the legend. Taken from ref. [6].

5 Summary and conclusions

From the analysis of the filtered multifragmentation data, all three terms in eq. (1), charged-particle kinetic energies, neutron kinetic energies and removal energy ($-Q$) are found to have significant weights in the excitation energy sum. In the upper panel of fig. 14 the relative kinetic-energy percentages are shown for LCPs, neutrons and IMFs as a function of E^*/A for ISiS data [6]. Neutrons and LCPs are roughly equivalent, each accounting for 20–30% over the entire E^*/A range. IMFs do not become significant until about $E^*/A \approx 3$–$4\,\mathrm{MeV}$, reaching a maximum of $\approx 10\%$ near $E^*/A \approx 6\,\mathrm{MeV}$. Above $E^*/A \approx 6\,\mathrm{MeV}$, all three percentages remain nearly constant. As is apparent from the previous discussions, these percentages vary, depending on assumptions about nonequilibrium emission, neutrons, etc.

The bottom frame of fig. 14 compares the percentage of the E^* sum for total kinetic-energy release with that for the removal energy derived from event reconstruction. For low excitation energies, the kinetic-energy sum and removal energy are roughly equivalent. One factor that tends to stabilize eq. (1) with respect to input assumptions is that some of the uncertainties are self-compensating. If, for example, the neutron multiplicity and/or energy input to the filter is too high, the separation energy decreases, and vice versa. Another factor that must be kept in mind is that many of the assumptions that are involved in the filter are averages, and therefore do not adequately account for fluctuations in the distributions. Because of the exponential decrease in yield with increasing E^*/A, fluctuations skew the distribution toward lower excitation energies. This effect is demonstrated in fig. 15. The upper frame shows the average yield as a function of E^*/A bin size (heavy solid line). Superimposed on each bin is a Gaussian approximation to the fluctuation widths which are assumed to increase with excitation energy (light lines). The effect on the E^*/A distribution is demonstrated in the middle frame of fig. 15, showing the yield (yellow on-

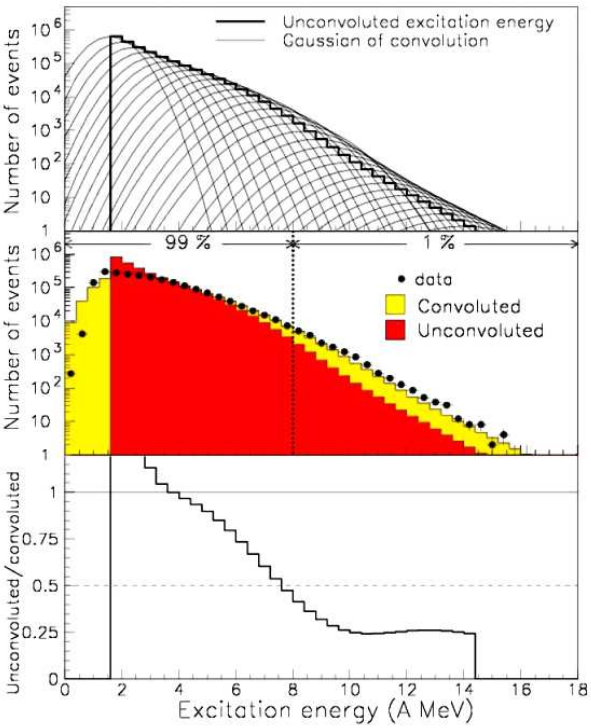

Fig. 15. Upper panel: Gaussian decomposition of the excitation energy distribution. Middle panel: comparison between the excitation energy distribution derived from calorimetry procedures and the deconvoluted distribution. Bottom panel: ratio of the deconvoluted distribution to original distribution. Taken from ref. [6].

line) for the data (solid points) and that for the deconvoluted distribution (red on-line). Over the range up to $E^*/A \approx 8\,\mathrm{MeV}$ there is relative agreement between the two distributions. Above this energy, the most probable E^*/A value increasingly falls below that of the average.

From examination of the existing analyses, it is estimated that as a thermodynamic variable, all of the results are self-consistent over about a 20% range in E^*/A. Given this uncertainty, however, there is general agreement among all of the data sets. In the range $E^*/A \approx 4$–$5\,\mathrm{MeV}$, a distinct change occurs in multifragmentation observables, indicating a change in the reaction mechanism. Within a phase transition scenario, this excitation energy would represent the liquid-gas transition energy. The consistency of the measurements is perhaps best illustrated by the caloric-curve analysis of Natowitz [34], in which all of the caloric-curve measurements are decomposed as a function of source mass. When this decomposition is performed, a systematic behavior is revealed that lends greater credence to the caloric-curve behavior in hot nuclear systems. To go beyond and thus relate quantitatively the experimental results to the nuclear equation of state, Z and A identification over a wide range would be needed.

References

1. J. Pochodzalla *et al.*, Phys. Rev. Lett. **75**, 1040 (1995).
2. R.T. de Souza *et al.*, contribution VI.1, this topical issue.
3. L. Pienkowski *et al.*, Phys. Lett. B **336**, 147 (1994).
4. F. Goldenbaum *et al.*, Phys. Rev. Lett. **77**, 1230 (1996).
5. K. Kwiatkowski *et al.*, Phys. Lett. B **433**, 21 (1998).
6. T. Lefort *et al.*, Phys. Rev. C **64**, 064603 (2001).
7. V. Radionov *et al.*, Nucl. Phys. A **700**, 457 (2002).
8. J.A. Hauger *et al.*, Phys. Rev. Lett. **62**, 024616 (2000).
9. J.A. Hauger *et al.*, Phys. Rev. C **57**, 764 (1998).
10. A. Schüttauf *et al.*, Nucl. Phys. A **607**, 457 (1996).
11. J.C. Steckmeyer *et al.*, Nucl. Phys. A **686**, 537 (2001); E. Vient *et al.*, Nucl. Phys. A **700**, 555 (2002).
12. R. Wada *et al.*, Phys. Rev. C **55**, 227 (1997); K. Hagel *et al.*, Phys. Rev. C **62**, 034607 (2000).
13. Y.G. Ma *et al.*, Nucl. Phys. A **749**, 106 (2005).
14. CHIMERA Collaboration (E. Galichet), private communication.
15. L. Beaulieu *et al.*, Phys. Rev. Lett. **77**, 462 (1996).
16. B. Djerroud *et al.*, Phys. Rev. C **64**, 034603 (2001).
17. M. D'Agostino *et al.*, Nucl. Phys. A **650**, 329 (1999).
18. M. D'Agostino *et al.*, Phys. Lett. B **473**, 219 (2000).
19. M. D'Agostino *et al.*, Nucl. Phys. A **699**, 795 (2002).
20. T. von Egidy *et al.*, Eur. Phys. J. A **8**, 197 (2000).
21. K.B. Morley *et al.*, Phys. Rev. C **54**, 737 (1996).
22. J. Łukasik *et al.*, Phys. Lett. B **566**, 76 (2003).
23. ALADiN Collaboration (W. Trautmann), private communication.
24. M.F. Rivet *et al.*, Phys. Lett. B **423**, 217 (1998); P. Desquelles *et al.*, Phys. Rev. C **62**, 024614 (2000).
25. Y. Perier *et al.*, Nucl. Instrum. Methods A **413**, 32 (1998).
26. J. Toke *et al.*, Phys. Rev. Lett. **75**, 2920 (1995).
27. A. Botvina, A.S. Ilijinov, I.N. Mishustin, Nucl. Phys. A **507**, 649 (1990).
28. D.H.E. Gross, Rep. Prog. Phys. **53**, 605 (1990).
29. R. Charity *et al.*, Nucl. Phys. A **483**, 371 (1998).
30. D. Durand, Nucl. Phys. A **541**, 266 (1992).
31. T. Lefort *et al.*, Phys. Rev. C **62**, 031604R (2000).
32. S.P. Avdeyev *et al.*, Nucl. Phys. A **709**, 392 (2002).
33. R.E.L. Green *et al.*, Phys. Rev. C **29**, 1806 (1984).
34. J.B. Natowitz *et al.*, Phys. Rev. C **65**, 034618 (2002); see also A. Kelić *et al.*, contribution V.2, this topical issue.